

Formation and collisional quenching of the long-lived $2s$ state of muonic hydrogen

V. P. Popov* and V. N. Pomerantsev†

Institute of Nuclear Physics, Moscow State University, 119992 Moscow, Russia

(Received 28 September 2010; published 30 March 2011; publisher error corrected 27 April 2011)

Ab initio study of the density-dependent population and lifetime of the long-lived $(\mu p)_{2s}$ and the yield of $(\mu p)_{1s}$ atoms with kinetic energy 0.9 keV have been performed. The direct Coulomb $2s \rightarrow 1s$ de-excitation is proved to be the dominant quenching mechanism of the $2s$ state at kinetic energy below $2p$ threshold and explain the lifetime of the metastable $2s$ state and high-energy 0.9 keV component of $(\mu p)_{1s}$ observed at low densities. The cross sections of the elastic, Stark, and Coulomb de-excitation processes have been calculated in the close-coupling approach taking into account both the closed channels and vacuum polarization shifts of the ns states. The cross sections are used as the input data in the detailed study of the atomic cascade kinetics. The theoretical predictions are compared with the known experimental data at low densities. The 47% yield of the 0.9 keV $(\mu p)_{1s}$ atoms is predicted for liquid-hydrogen density.

DOI: 10.1103/PhysRevA.83.032516

PACS number(s): 36.10.Ee

I. INTRODUCTION

Exotic hydrogenlike atoms are formed in highly excited states after slowing down and Coulomb capture of heavy negative particles (μ^- , π^- , etc.) in hydrogen media. The further evolution of their initial distributions in quantum numbers and kinetic energy are defined by the radiative transitions and collisional-induced processes during the so-called atomic cascade. The experimental data, such as the yields of the x ray and the products of the weak or strong interaction of the exotic particle in the low angular-momentum states with hydrogen isotopes, are mainly related to the last stage of the atomic cascade.

A number of experiments in which the energy distributions of $\mu^- p$, $\mu^- d$, and $\pi^- p$ atoms were measured using various time-of-flight methods [1–5] showed that the kinetic energy of the exotic atoms changes during the cascade. In particular, the existence of high-energy components has been established in pionic hydrogen in the neutron time-of-flight experiment [3] and in muonic hydrogen in diffusion experiments [4,5]. These experiments as well as the precision spectroscopic experiments [6–8] require a more sophisticated approach to a proper description of the atomic cascade taking into account the evolution of their distributions on both the quantum numbers and kinetic energy. In particular, the theoretical kinetic energy distributions of the np states at the instant of the radiative $np \rightarrow 1s$ transitions must be taken into account for the reliable description of the Doppler broadening of the K lines obtained from experiments (see [8] and references therein). Thus a good understanding of the kinetics of atomic cascade in hydrogenlike exotic atoms is very important both for the planning and interpretation of experiments (e.g., see for a review [9]).

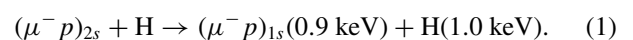
Muonic hydrogen, $(\mu^- p)$, being analogous to an ordinary hydrogen atom, is of special interest among the exotic atoms due to its simplest structure and provides the opportunity for the investigation of a number of problems, such as the exotic atom physics, quantum electrodynamics, weak interaction,

and atomic scattering processes. In particular, the study of $(\mu^- p)$ atom in the $2s$ state plays a particular role due to the $(2s_{1/2}-2p_{1/2})$ Lamb shift, $E_L = 202.0$ meV [10], and has no analog in hadronic (pionic, kaonic, etc.) atoms in which strong interaction leads to nuclear absorption or annihilation from this state.

Recently, the first measurement of the E_L was performed in the precision μp Lamb shift experiment and the root-mean-square charge radius of the proton was found with a relative accuracy better than 10^{-3} [11]. The precision knowledge of the proton radius has fundamental meaning for both the baryon structure and the bound-state QED. The success of this experiment crucially depended upon the population $\epsilon_{2s}^{\text{long}}$ and lifetime τ_{2s}^{long} of the *metastable or long-lived* fractions of the $2s$ state at kinetic energy below E_L . The existence of this fraction was experimentally proved [12,13] by discovering a high-energy component of $(\mu p)_{1s}$ with kinetic energy ~ 0.9 keV in the analysis of the time-of-flight spectra (at low gas pressures $p_{\text{H}_2} = 16$ and 64 hPa). The origin of this component was attributed to the nonradiative quenching of the long-lived $2s$ state due to the formation of the muonic molecule in a resonance $(\mu p)_{2s} + \text{H}_2$ collision and subsequent Coulomb de-excitation of the $(pp\mu)^+$ complex—the so-called side path model [14–16]. However, a theoretical estimation of the nonradiative quenching rate, $\lambda_{2s}^{\text{quench}}$, in the framework of this model [16] gives $\lambda_{2s}^{\text{quench}} \sim 5 \times 10^{10} \text{ s}^{-1}$ at liquid-hydrogen atom density [(LHD) $N_{\text{LHD}} = 4.25 \times 10^{22} \text{ atoms/cm}^3$] that is about an order of magnitude less than the value $\lambda_{2s}^{\text{quench}} = 4.4_{-1.8}^{+2.1} \times 10^{11} \text{ s}^{-1}$ deduced from the experimental data [13].

It is worthwhile noting that no manifestations of the above resonance mechanism were found in experiments (e.g., see [3,7,8]). In particular, in the experimental work [8] no evidence of the molecular formation [15,16] was found at the 1% level for $3p-1s$ line broadening in the muonic atom except the Coulomb de-excitation process.

In the paper [17] we suggested that the observed collisional quenching of the metastable $2s$ state and high-energy $(\mu p)_{1s}$ component can be explained by the direct Coulomb de-excitation (CD) process,



*popov@nucl-th.sinp.msu.ru

†pomeran@nucl-th.sinp.msu.ru

However, the problem of the $(\mu p)_{2s}$ metastability has not been the subject of the paper [17].

The main motivation for the present paper was to confirm our previous suggestion [17] that the direct CD $2s \rightarrow 1s$ is the dominant mechanism of the collisional quenching of the $(\mu^- p)_{2s}$ at kinetic energy below the $2s$ - $2p$ threshold. In the present study this suggestion is confirmed by the *ab initio* fully quantum-mechanical calculations of the cross sections for the elastic scattering, Stark transitions and CD within the close-coupling approach (CCA) taking into account the closed channels and the ns - np energy shifts of the muonic hydrogen levels.

According to our knowledge, the cross sections for the CD process (1) and elastic $2s \rightarrow 2s$ scattering at the subthreshold region were not calculated until now. The values of these cross sections enable one to explain the experimental quenching rate of the long-lived $2s$ state quantitatively. The calculated cross sections of the above-mentioned processes have been used in the detailed calculations of the atomic cascade kinetics. The population and lifetime of the metastable $2s$ state, as well as the yield $\epsilon_{1s}^{\text{hot}}$ of the hot (0.9 keV) component of the $(\mu^- p)_{1s}$ over a wide range of the relative density $\varphi = N/N_{\text{LHD}}$ from 10^{-9} up to 1 are predicted. The preliminary results based on our theoretical cross sections obtained in the middle of 2008 are published in [18]. As compared with [18], the more elaborate calculations of the elastic $2s \rightarrow 2s$ scattering and CD $2s \rightarrow 1s$ cross sections below $2p$ threshold have been performed focusing on the convergence of the cross sections with increasing the number of the basis states, thus the reliability of our theoretical predictions has been significantly improved in the present study.

The paper is organized as follows. The brief outline of the close-coupling approach is described in Sec. II. The calculated cross sections and the rates of the elastic scattering, Stark transitions, and Coulomb de-excitation of the muonic atom in the state with $n = 2$ are presented in Sec. III. The cascade model and the definition of the initial n , l , and E distributions are described in Sec. IV. The results of the cascade calculations for the energy distributions of muonic hydrogen in $1s$ and $2s$ states at low densities, density dependence of the arrival $2s$ population, population and lifetime of the metastable $2s$ fraction, and also the yield of the hot $(\mu^- p)_{1s}$ are presented in Sec. V. The main results of the paper are summarized in Sec. VI.

Atomic units [$\hbar = e = m_e m_b / (m_e + m_b) = 1$] are used throughout the paper unless otherwise stated.

II. CLOSE-COUPPING APPROACH

In the present paper we use the close-coupling approach (CCA), in which the scattering processes,

$$(\mu^- p)_{nl} + H \rightarrow (\mu^- p)_{n'l'} + H, \quad (2)$$

such as elastic scattering ($n' = n, l' = l$), Stark transitions ($n' = n, l' \neq l$), and CD ($n' < n$) are described in a unified manner. This approach was applied earlier by the authors for the quantum-mechanical treatment of elastic scattering, Stark transitions and CD in the collisions of excited exotic (muonic, pionic, and antiprotonic hydrogen) atoms with hydrogen ones

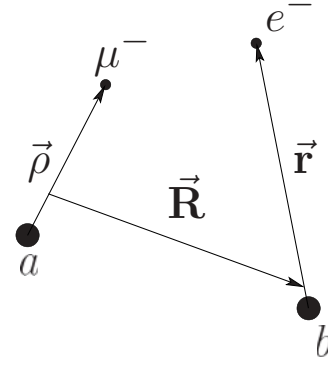


FIG. 1. The Jacobi coordinates used for the system $(\mu^- a + be^-)$. \mathbf{R} is a vector from the center of mass of $(\mu^- a)$ to the center of mass of (be^-) (a and b are nuclei of muonic and ordinary atoms—in the present case, protons).

[17,19–22] and the hydrogen molecules [23]. Here, we briefly remind the main assumptions and outline of the CCA.

The nonrelativistic Hamiltonian for the four-body system $(a + \mu^- + b + e^-)$, after separating the center-of-mass motion, can be written in Jacobi coordinates $(\mathbf{R}, \boldsymbol{\rho}, \mathbf{r})$ (see Fig. 1) as

$$H = -\frac{1}{2M} \Delta_{\mathbf{R}} + h_{\mu}(\boldsymbol{\rho}) + h_e(\mathbf{r}) + V(\mathbf{r}, \boldsymbol{\rho}, \mathbf{R}), \quad (3)$$

where M is the reduced mass of the system, and h_{μ} and h_e are the Hamiltonian of the free muonic and ordinary hydrogen atoms. The electrostatic interaction between the subsystems $V(\mathbf{r}, \boldsymbol{\rho}, \mathbf{R})$ is the sum of four two-body Coulomb interactions:

$$\begin{aligned} V(\mathbf{r}, \boldsymbol{\rho}, \mathbf{R}) &= V_{ab} + V_{\mu b} + V_{ae} + V_{\mu e}, \\ V_{ab} &= \frac{1}{r_{ab}} = |\mathbf{R} + \nu \boldsymbol{\rho} - \nu_e \mathbf{r}|^{-1}, \\ V_{\mu b} &= -\frac{1}{r_{\mu b}} = -|\mathbf{R} - \xi \boldsymbol{\rho} - \nu_e \mathbf{r}|^{-1}, \\ V_{\mu e} &= \frac{1}{r_{\mu e}} = |\mathbf{R} - \xi \boldsymbol{\rho} + \xi_e \mathbf{r}|^{-1}, \\ V_{ae} &= -\frac{1}{r_{ae}} = -|\mathbf{R} + \nu \boldsymbol{\rho} + \xi_e \mathbf{r}|^{-1}, \end{aligned} \quad (4)$$

where ν , ξ , ν_e , and ξ_e are defined as follows: $\nu = m_{\mu} / (m_{\mu} + m_a)$, $\xi = m_a / (m_{\mu} + m_a)$, $\nu_e = m_e / (m_e + m_b)$, $\xi_e = m_b / (m_e + m_b)$ (m_a, m_b, m_{μ} , and m_e are the masses of hydrogen isotopes, muon, and electron, respectively).

Since the muonic atom is neutral and in the low-lying states much smaller than the target molecule, the distortion of the target electron structure during collision can be neglected. Moreover, the $(\mu^- p)_{nl} - \text{H}_2$ collisions can be approximately treated as the $(\mu^- p)_{nl} - \text{H}$ scattering. These assumptions are supported, in particular, by a good agreement of the experimental data [3] and our theoretical results [24] for the kinetic energy distribution of $\pi^- p$ atoms at the instant of nuclear absorption. The effect of the electron density difference near proton in the hydrogen molecule as compared with that in hydrogen atom was estimated by using the one-electron function obtained in the framework of the improved Heitler-London method [25]. Our calculations show that the

main effect is a weak suppression of the elastic and Stark cross sections above the $2p$ threshold. Furthermore, since Lamb shifts of the ns states are about two order of magnitude more than both the fine and hyperfine splittings, the muonic atom states are described by the nonrelativistic hydrogenlike wave functions with the energies of ns states shifted with respect to the degenerate (nl ; $l \neq 0$) states. In addition, in the present consideration we use the “frozen” electron approximation assuming that the hydrogen atom remains in the ground state during the collision. CCA can be extended in a straightforward manner to include also the target electron excitations.

Thus, the basis states are constructed from the hydrogenlike wave functions of electron $|1s\rangle$, muon $|nl\rangle$, and the eigenfunctions $|L\lambda\rangle$ of the angular momentum for the relative motion:

$$|1s, nl, L : JM\rangle \equiv \frac{1}{\sqrt{4\pi}} R_{1s}(r) R_{nl}(\rho) \mathcal{Y}_{lL}^{JM}(\hat{\rho}, \hat{\mathbf{R}}), \quad (5)$$

where

$$\mathcal{Y}_{lL}^{JM}(\hat{\rho}, \hat{\mathbf{R}}) \equiv i^{l+L} \sum_{m\lambda} \langle lmL\lambda | JM \rangle Y_{lm}(\hat{\rho}) Y_{L\lambda}(\hat{\mathbf{R}}). \quad (6)$$

Here, the orbital angular momentum \mathbf{l} of the muonic atom is coupled with the orbital momentum \mathbf{L} of the relative motion to give the total angular momentum $\mathbf{J} = \mathbf{l} + \mathbf{L}$.

The total wave function of the system in the state with the total energy E , definite quantum numbers of the total angular momentum (JM), and parity $\pi = (-1)^{l+L}$ is expanded in terms of the basis states $|1s, nl, L : JM\rangle$ as follows:

$$\Psi^{EJM\pi}(\mathbf{r}, \rho, \mathbf{R}) = R^{-1} \sum_{nlL} G_{nlL}^{EJ\pi}(R) |1s, nl, L : JM\rangle. \quad (7)$$

The expansion (7) leads to the close-coupling second-order differential equations for the radial functions of the relative motion $G_{nlL}^{EJ\pi}(R)$:

$$\begin{aligned} & \left(\frac{d^2}{dR^2} + k_{nl}^2 - \frac{L(L+1)}{R^2} \right) G_{nlL}^{EJ\pi}(R) \\ & = 2M \sum_{n'l'L'} W_{nlL, n'l'L'}^{J\pi}(R) G_{n'l'L'}^{EJ\pi}(R), \end{aligned} \quad (8)$$

where $k_{nl}^2 = 2M(E_{\text{c.m.}} - \Delta\varepsilon_{nl, n_1 l_1})$ specifies the channel wave number. In the present study we use the basis sets in which both the open ($k_{nl}^2 > 0$) and closed ($k_{nl}^2 < 0$, $\text{Im } k_{nl} > 0$) channels have been included. $E_{\text{c.m.}}$ is the relative motion energy in the entrance ($n_1 l_1$) channel and $\Delta\varepsilon_{nl, n_1 l_1}$ is the threshold of the current (nl) channel referring to the entrance channel threshold:

$$\Delta\varepsilon_{nl, n_1 l_1} = \varepsilon_{nl} - \varepsilon_{n_1 l_1}.$$

Here, ε_{nl} is the bound-state energy of the muonic atom with Lamb shift¹ $\varepsilon_n^{\text{Lamb}}$ taken into account:

$$\varepsilon_{nl} = -0.5\mu/n^2 - \delta_{l0}\varepsilon_n^{\text{Lamb}},$$

where $\mu = m_\mu m_a / (m_\mu + m_a)$ is the reduced mass of the muonic atom.

Finally, $W_{nlL, n'l'L'}^J$ are the matrix elements of the interaction potential (4) over the basis states:

$$\begin{aligned} & W_{n'l'L', nlL}^{J\pi}(R) \\ & = \langle 1s, n'l', L' : JM | V(\mathbf{r}, \rho, \mathbf{R}) | 1s, nl, L : JM \rangle. \end{aligned} \quad (9)$$

These matrix elements are obtained by averaging the potential (4) over the electron wave function $|1s\rangle$ and subsequently applying the addition theorem for the spherical Bessel functions. The integration over $(\rho, \hat{\mathbf{R}})$ with the muon hydrogenlike functions reduces the matrix element (9) to the multiple *finite* sum (for details see [21]).

The total number of coupled equations in the system (8) is defined by the set of the principal quantum numbers n of the states included in the calculation. For every n the number of the coupled channels N_n is equal to $n(n+1)/2$ if parity $\pi = (-1)^{l+L}$ coincides with $(-1)^J$, and $n(n-1)/2$ otherwise. The basis sets including all the μ^-p states with $n = 1 - n_{\text{max}}$ were used in our calculations, so the total number of coupled Eqs. (8) is equal to $N = \sum_{n=1}^{n_{\text{max}}} N_n$.

The radial functions $G_{nlL}^{EJ\pi}(R)$ should be regular everywhere and behave as $\sim R^{L+1}$ at $R \rightarrow 0$. At asymptotic distances ($R \rightarrow \infty$) one can use the usual standing-wave boundary conditions involving the real symmetrical K matrix. K matrix is related to T matrix by the equation $T = 2iK(1 - iK)^{-1}$.

In order to find the K and thereby T matrix one does not need to know the wave functions $G_{nlL}^{EJ\pi}(R)$ themselves. It is possible to define the K matrix using only the ratios of these functions at the two nearest points R and $R+h$:

$$D(R) = G(R)G^{-1}(R+h),$$

where h is the integration step. The main advantage of such an approach is that the propagation matrix D is limited even for the closed channels, where functions $G(R)$ can exponentially increase. So, it is possible to treat both open and closed channels in a unified manner. In all our calculations of the cross sections we used such a propagation matrix method (PMM) the details of which are given in Appendix.

The partial-wave on-shell amplitude for the transition $nlm \rightarrow n'l'm'$ is defined by the T matrix:

$$\begin{aligned} f_{nlm}^{n'l'm'}(E, \hat{\mathbf{k}}_{nl}, \hat{\mathbf{R}}) & = \frac{2\pi i}{\sqrt{k_{nl} k_{n'l'}}} \sum_{LL'M\lambda\lambda'} i^{L'-L} \langle lmL\lambda | JM \rangle \\ & \times \langle l'm'L'\lambda' | JM \rangle Y_{L\lambda}^*(\hat{\mathbf{k}}_{nl}) Y_{L'\lambda'}(\hat{\mathbf{R}}) T_{nlL \rightarrow n'l'L'}^J(E). \end{aligned} \quad (10)$$

The partial-wave differential and integral cross sections of the processes (2) for the transitions $nl \rightarrow n'l'$, averaged over an initial and summed over the final sublevels, are given by

$$\frac{d\sigma_{nl \rightarrow n'l'}^J(E)}{d\Omega} = \frac{k_{n'l'}}{k_{nl}} \frac{1}{2l+1} \sum_{m, m'} |f_{nlm}^{n'l'm'}(E, \hat{\mathbf{k}}_{nl}, \hat{\mathbf{R}})|^2, \quad (11)$$

and

$$\sigma_{nl \rightarrow n'l'}^J(E) = \frac{\pi}{k_{nl}^2} \frac{2J+1}{2l+1} \sum_{LL'} |T_{nlL \rightarrow n'l'L'}^J(E)|^2. \quad (12)$$

The total integral cross section is the sum of the partial ones:

$$\sigma_{nl \rightarrow n'l'}(E) = \sum_J \sigma_{nl \rightarrow n'l'}^J(E). \quad (13)$$

¹We use the value $\varepsilon_2^{\text{Lamb}} = 0.202$ eV [10] for $n = 2$ and approximated values $\varepsilon_n^{\text{Lamb}} = \varepsilon_2^{\text{Lamb}}(2/n)^3$ for $n > 2$.

III. RESULTS OF THE CALCULATIONS WITHIN CC APPROACH. EFFECT OF CLOSED CHANNELS.

The CCA calculations of the differential and integral cross sections of the processes (2) have been performed for the states with $n = 2 - 8$ at the energy range from $E_{c.m.} = 0.0001$ eV up to the maximal possible energies originating from Coulomb de-excitation. Summation over the partial waves in Eq. (13) has been done up to the value J_{max} until an accuracy better than 0.1% was reached at all energies.

According to our study, the closed-channel effects are more pronounced for the processes in the lower states ($n = 2 - 5$) at very low collision energies, especially near and below $ns-np$ thresholds. Here we present some of our results for the $2l \rightarrow 2l'$ (elastic and Stark scattering) and CD $2s, 2p \rightarrow 1s$ transitions where the effects of the closed channels are the most significant and extremely important for the problem of collisional quenching of the metastable $2s$ state.

A. Convergence of the close-coupling calculations with extending basis

The key point in the present work is the calculations of the elastic and CD cross sections for $(\mu^- p)_{2s} + H$ collisions at low-energy range $E_{c.m.} = (0.0001 - 0.202)$ eV [i.e., below the $(2s-2p)$ threshold]. Just these cross sections determine the collisional quenching of the metastable fraction of the muonic $2s$ state. They are very sensitive to the short-range behavior of the interaction and therefore to the dimension of the basis used in the calculations. On the other hand, as our present calculations show, only the three lowest partial waves with $J = 0, 1, 2$ contribute to the above-mentioned cross sections at kinetic energies below $(2s-2p)$ threshold. This enables us to study the convergence of results with the extension of the basis set in more detail.

Figure 2 shows the calculated total CD cross section $\sigma_{2s \rightarrow 1s}$ as a function of the laboratory kinetic energy E_{lab} .

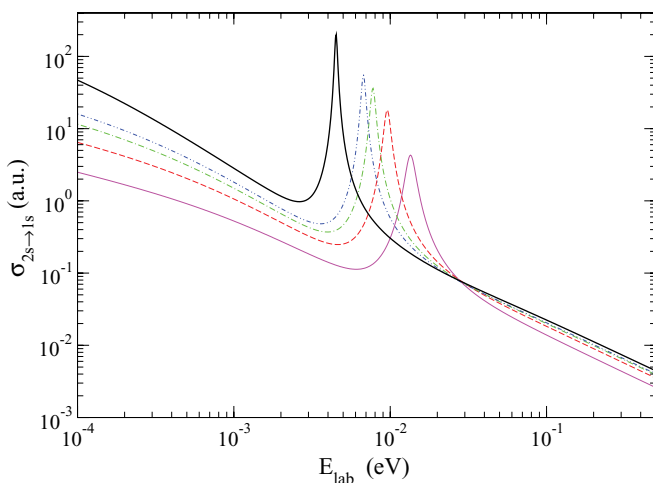


FIG. 2. (Color online) Coulomb de-excitation $2s \rightarrow 1s$ cross sections versus laboratory kinetic energy calculated with different basis sets including all the $(\mu^- p)$ states up to $n = n_{max}$: $n_{max} = 15$ (thin solid line), $n_{max} = 20$ (dashed line), $n_{max} = 25$ (dashed-dotted line), $n_{max} = 30$ (double-dot-dashed line). The results of the extrapolation to $n_{max} \rightarrow \infty$ are shown by a thick solid line.

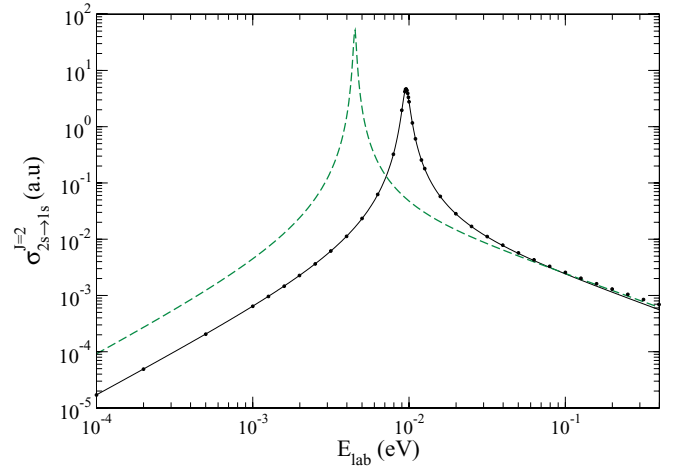


FIG. 3. (Color online) The partial-wave CD cross sections $\sigma_{2s \rightarrow 1s}^{J=2}$ calculated with the $n_{max} = 20$ basis set (circles) and its approximation by Eq. (14) (solid line). The dashed line shows the result of extrapolation of this cross section to $n_{max} \rightarrow \infty$.

The calculations have been performed in CCA using the different basis sets including all the $(\mu^- p)$ states with the values of the principal quantum number n from 1 up to $n_{max} = 15, 20, 25, 30$. As it is seen from Fig. 2, the energy behavior of the cross section changes in a regular manner with the extension of the basis set. The only resonance structure at the subthreshold region appears in the D wave. This resonance manifests also in the elastic $2s-2s$ and $1s-1s$ cross sections. With increasing n_{max} it becomes narrower and moves toward the $2s$ threshold. The presence of this resonance appreciably increases the cross sections and thereby affects the lifetime of the metastable fraction. It is therefore important to determine whether this resonance survives with a further unlimited extension of the basis. To clarify this, the calculated partial-wave cross sections at the subthreshold region for $J = 0, 1, 2$ (for each of the above-mentioned basis sets) were approximated by the analytical functions with three to four parameters which were fitted using the least-squares method. Furthermore, assuming that the obtained parameters are the analytical functions of n_{max} , we extrapolated their values to the limit $n_{max} \rightarrow \infty$ by means of Pade approximants. The cross sections obtained by this extrapolation correspond to the calculation taking into account all the infinite discrete spectrum of the muonic atom.²

For example, the partial-wave CD cross section for $J = 2$ calculated with the $n_{max} = 20$ basis set (circles) and its analytical approximation (solid line) are shown in Fig. 3 as a function of the laboratory energy. For analytical approximation we applied the four-parameter formula which describes both the resonance (in Breit-Wigner form) and correct threshold behavior of the CD cross section ($\sigma_{CD}^J \sim E^{J-1/2}$; here $L = J$):

$$\sigma_{2s \rightarrow 1s}^{J=2} = \frac{20\pi(2mE_{lab})^{3/2}}{\sqrt{1+bE_{lab}}} \frac{(\gamma)^2}{(E_{lab} - E_0)^2 + (\Gamma)^2} \quad (14)$$

²The effect of the continuous spectrum of the muonic atom is not considered in the present study. According to our preliminary estimation the continuum contribution does not exceed 10%.

($m = m_\mu + m_a$ is the mass of muonic atom). Two of these four parameters, namely E_0 and Γ , correspond to the position of the resonance and its width, respectively. The extrapolated cross section $\sigma_{2s \rightarrow 1s}^{J=2}$ calculated by the formula (14) with extrapolated values of the parameters,

$$E_0 = 4.5 \text{ meV}, \quad \Gamma = 0.095 \text{ meV},$$

is shown in Fig. 3 by the dashed line. The similar procedure (but with the other formulas) was used for the $n_{\max} \rightarrow \infty$ extrapolation of the $J = 2$ elastic cross section and also both elastic and CD cross sections with $J = 0$ and 1. Here, we give also the used formulas for the analytical approximation of the partial CD cross sections:

$$J = 1,$$

$$\sigma_{2s \rightarrow 1s}^{J=1} = 3\pi \sqrt{2m E_{\text{lab}}} \frac{b_0}{1 + b_1(2m E_{\text{lab}})^{3/2}}, \quad (15)$$

and $J = 0$,

$$\sigma_{2s \rightarrow 1s}^{J=0} = \frac{\pi}{\sqrt{2m E_{\text{lab}}}} \frac{a_0(1 + a_1\sqrt{2m E_{\text{lab}}})}{1 + a_2 2m E_{\text{lab}}}. \quad (16)$$

The total CD $2s \rightarrow 1s$ cross section at the subthreshold region obtained as a result of such extrapolations for the partial CD cross sections is shown in Fig. 2 by a thick solid line.

B. Collision rates for $(\mu^- p)_{n=2} + H$ processes

Here, we present the results of the calculations for the $(\mu^- p)_{n=2} + H$ collision rates,

$$\lambda_{nl \rightarrow n'l'}(E_{\text{lab}}) = N_{\text{LHD}} \varphi \sigma_{nl \rightarrow n'l'}(E_{\text{lab}}) \sqrt{\frac{2E_{\text{lab}}}{m}},$$

where $\varphi = N/N_{\text{LHD}}$ is the relative density of the target.

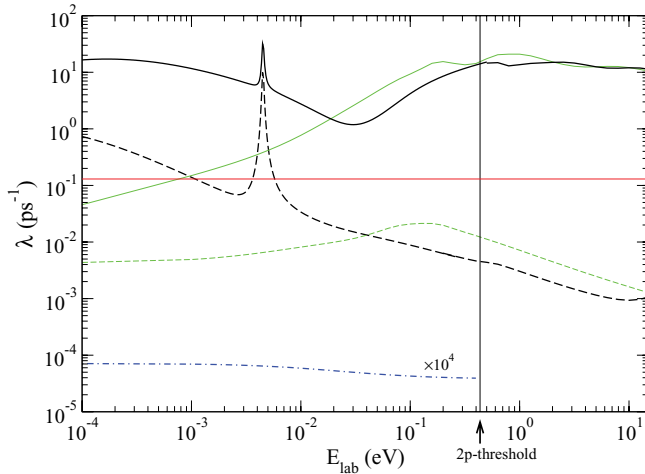


FIG. 4. (Color online) Collisional rates for the elastic $2s \rightarrow 2s$ (solid lines) and CD $2s \rightarrow 1s$ (dashed lines) processes versus laboratory kinetic energy at LHD. The thin lines correspond to the calculations of the cross sections with the basis including only the $(\mu^- p)$ states with $n_{\max} = 2$; the results obtained with the extended basis sets and subsequent extrapolation to $n_{\max} \rightarrow \infty$ are shown by thick lines (see text). For comparison the dashed-dotted line shows the $2s \rightarrow 1s$ rate (multiplied by 10^4) calculated below the $2p$ threshold without the closed channels at all. The vertical line shows the value of the $2p$ threshold ($E_{\text{thr}} = 0.435$ eV in the laboratory system). The radiative $2p$ - $1s$ rate is shown with a horizontal line.

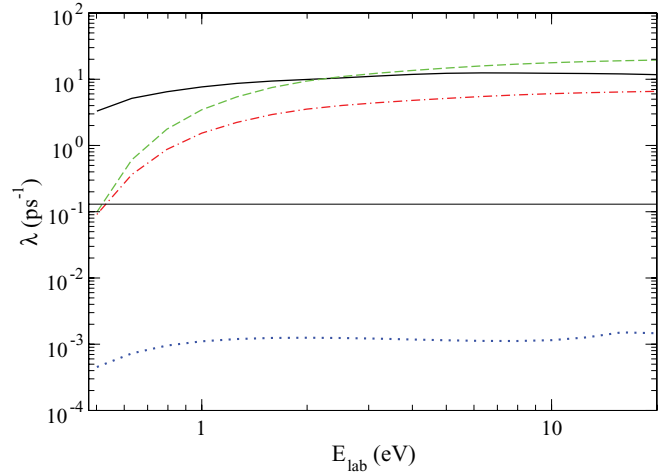


FIG. 5. (Color online) Collisional rates for the elastic $2p \rightarrow 2p$ (solid line), Stark ($2s \rightarrow 2p$ (dashed line), $2p \rightarrow 2s$ (dashed-dotted line), and CD $2p \rightarrow 1s$ (dotted line) processes. The energy is referred to as the $2s$ threshold. The horizontal line is the radiative $2p$ - $1s$ rate.

Figures 4 and 5 show the collisional rates at LHD as a function of the laboratory kinetic energy. The corresponding cross sections have been calculated with the different basis sets: the minimal basis ($n_{\max} = 2$), the extended basis ($n_{\max} \rightarrow \infty$), as discussed above, and (for comparison) the basis without the closed channels at all (see dashed-dotted line in Fig. 4). As is seen from Fig. 4, the proper description of the collisional processes is impossible in the subspace of the open channels. The inclusion of the nearest weakly closed $2p$ state into basis leads to the tremendous increase of both the elastic $2s \rightarrow 2s$ and CD $2s \rightarrow 1s$ rates (about 10^3 and 10^6 times, respectively). The inclusion of the $2p$ state into the basis allows one partially to take into account the “long-range dipole polarization” of the muonic atom, which gives the main contribution to both the elastic and CD cross sections and to ensure their correct threshold behavior (there is no discontinuity at the $2p$ threshold; see Fig. 4).

According to the present study, the minimal basis set including the open $1s$, $2s$ states and the nearest weakly closed $2p$ state is also not sufficient (see Fig. 4) for the proper description of the elastic and CD cross sections below the $2p$ threshold. A more reliable description in this energy region can be reached with the extended basis set including strongly closed channels with $n \geq 3$. Such an extension of the basis allows one more entirely to take into account the polarization of the muonic hydrogen.

At energies above the $2p$ threshold the contribution of the higher partial waves to the elastic cross section becomes more essential and the details of the short-range interaction at $R < 0.5$ a.u. (the closed channel effects) are less important. The corresponding rates of the elastic $2s \rightarrow 2s$ scattering calculated in the basis with $n_{\max} = 2$ and in the extended basis ($n_{\max} = 10$) are in very good agreement at kinetic energy above ~ 2 eV. In contrast, the CD process is accompanied by a large energy release (e.g., about 2 keV in $2s \rightarrow 1s$ transition) and occurs at substantially smaller distances, so the details of the short-range interaction play an important role also above the $2p$ threshold. In addition, the number of partial

waves involved in the CD process is always essentially less than in the elastic and Stark scattering—the large centrifugal barrier (for higher partial waves) prevents the exotic atom from reaching the interaction range relevant for the CD process. Thus, the closed-channel effect is practically negligible for the elastic and Stark scattering above the $2p$ threshold and is less pronounced for the CD process than at the subthreshold region (see Fig. 4).

Since the ratios between the rates of collisional processes are independent from the target density, the useful observations can be derived from the results presented in Figs. 4 and 5 without the atomic cascade calculations. The CD $2p \rightarrow 1s$ is strongly suppressed in comparison with the other cascade processes and can be neglected in kinetics calculations. In contrast, the rate of the $2s \rightarrow 1s$ CD at kinetic energy below a few tens meV becomes less suppressed as compared with the rate of the elastic $2s \rightarrow 2s$ scattering; therefore, the CD $2s \rightarrow 1s$ process can quench the metastable $2s$ state. It is also clear that the formation of the metastable $2s$ state cannot lead to the fast CD $2s \rightarrow 1s$ transition before the muonic hydrogen is thermalized. Finally, the comparison of the CD $2s \rightarrow 1s$ rate with the rate of muon decay allows us to conclude that the lifetime of the metastable $2s$ state at densities less than $\sim 10^{-6}$ is mainly defined by the muon lifetime while at higher densities the situation is quite different and the detailed kinetics calculations are needed.

IV. CASCADE MODEL

A. Outline of cascade model

The exotic atom formation is followed by a number of successive radiative and collisional de-excitation processes, forming the so-called atomic cascade, until the exotic atom arrives at the ground state or the weak decay of the exotic particle occurs. In the case of hadronic atoms, the cascade can be also terminated by strong absorption or annihilation processes. The first theoretical study of the atomic cascade was performed about 50 years ago by Leon and Bethe [26]. In this and subsequent papers [27,28], the rates of the collisional processes were calculated in the semiclassical approximation for a fixed value of kinetic energy about 1 eV and used for the simulation of the atomic cascade with employing different free parameters (e.g., the scaling factors for the rates of Stark transitions, CD, and the Auger process, and also the value of kinetic energy of the exotic atom).

In the present paper we use the so-called extended standard cascade model (ESCM) which includes all the known processes (radiative, Auger and Stark transitions, elastic scattering, and Coulomb deexcitation) and takes into account the evolution of the kinetic energy during the cascade. The ESCM originally developed by Markushin [29] was later essentially improved (see [30] and references therein) and recently in the paper [24]. The improvements were mainly achieved due to the new theoretical results [19,20,22,31] for the cross sections of the collisional processes.

The cascade in the exotic atoms in [30] is divided into classical ($n > 7$) and quantum-mechanical ($n \leq 7$) domains. In the classical domain the results of the classical-trajectory Monte Carlo calculations for the collisions of highly excited

exotic atoms with molecular hydrogen were used to obtain the rates of the elastic scattering, Stark mixing, and CD processes. In the quantum-mechanical domain, the authors of [30] used the new results for the elastic and Stark cross sections calculated (for $n = 2-5$) in the close-coupling approach [31] at energies above np thresholds and the parametrization of the semiclassical results [32] for the CD cross sections, assuming that their angular distributions are isotropic. The cross sections of the external Auger were calculated [31] in the semiclassical approximation and used through the whole cascade.

In the present version ESCM as well as in our recent paper [24] the description of the classical domain are similar to [30] but the boundary of the classical domain is defined by the condition $n > 8$. In the quantum-mechanical domain ($n \leq 8$), the differential and integral cross sections for the elastic scattering, Stark, and CD transitions $nl \rightarrow n'l'$ calculated simultaneously within the present version of the CCA with the extended basis set including the closed channels have been used. Thus, the new cascade code does not employ any fitting parameters and additional assumptions concerning the collisional cross sections. The new collisional rates, especially for the CD process, lead to a significant improvement of the results of our cascade studies compared with the previous ones and allow us more reliably to describe the evolution of kinetic energy during the cascade (see [8,24]).

The thermal motion of the target is also taken into account in the present cascade calculations. To describe the thermal motion of the target the Maxwell distribution was used:

$$W(E_t, E_0) = 3 \sqrt{\frac{3E_t}{2\pi E_0^3}} \exp\left(\frac{-3E_t}{2E_0}\right). \quad (17)$$

Here E_t is the energy of the target atom and $E_0 \cong 0.0135$ eV is the parameter corresponding to the mean kinetic energy of the hydrogen atom at the temperature of the target ($T = 300$ K) in diffusion experiments [12].

B. Initial (n, l, E) distributions

For the realistic study of atomic cascade it is necessary to establish both the initial states from which the processes occur and the initial kinetic energy of the exotic atom. These initial conditions for the cascade calculations are defined by the distributions of exotic atoms in the quantum numbers (n, l) and laboratory kinetic energy E_{lab} at the instant of their formation. The knowledge of these distributions is especially important for the description of the cascade at low target densities.

As a rule, in the previous cascade calculations the simplest picture of the exotic atom formation is used: the initial principal quantum number is fixed at $n = n_0 \approx \sqrt{\mu}$ (~ 14 for the muonic hydrogen atom), and the statistical l distribution $F(l_0) = (2l_0 + 1)/n_0^2$ is assumed.

More elaborate studies [33–36] of the exotic atom formation taking into account the molecular structure of the target result in the initial n distribution with the sharp peak at lower values of the principal quantum number (for muonic hydrogen at $n_0 \cong 11$) and nonstatistical l distribution.

In the limit of the lowest relative densities $\varphi \lesssim 10^{-7}$ the atomic cascade is mainly determined by the muon lifetime and the rates of radiative transitions; therefore, the information

about the initial E and (n, l) distributions is conserved up to the end of the cascade and can be obtained from the relative K -line yields (Y_i , $i = \alpha, \beta$, etc.) and the kinetic energy distribution of muonic atoms in the $1s$ state. We assume that those distributions are factorized and can be considered independently.

Since the relative $K\alpha$ -line yield is experimentally determined with more precision than the yields of the higher lines and at low target densities mainly depends on the population of the circular l sublevels, we use this knowledge to study the initial n and l distributions. In addition, at low density the relative K yields weakly depend on the kinetic energy distribution at the moment of the radiative transition. In the present paper we choose the Gaussian n distribution,

$$F_n = N_n \exp[-\alpha_n(n - n_0)^2], \quad (18)$$

centered at $n_0 = 11$ with $\alpha_n = 0.5$, and the modified statistical l distribution,

$$F_l = N_l (2l + 1) \exp[-\alpha_l(2l + 1)], \quad (19)$$

where N_n and N_l are normalization constants.

The calculated relative $K\alpha$ -line yield is shown in Fig. 6 in comparison with the experimental data [37–39]. The theoretical results illustrate the effect of the initial l distribution at the fixed n distribution (18). It is seen that the statistical l distribution ($\alpha_l = 0$, dashed line) results in contradiction with the experimental data at densities $\varphi \lesssim 10^{-5}$, systematically increasing the relative yield of $K\alpha$ line in comparison with the experimental data. These differences (most pronounced at densities below 10^{-6}) cannot be explained by the possible uncertainties in the rates of the collisional processes and are due to the initial nonstatistical l distribution. Indeed, at the lowest densities the cascade is purely radiative and in case of the statistical initial l distribution the relative $K\alpha$ yield must be practically equal to 1 due to the selection rules in the radiative transitions (the radiative transitions with $\Delta l = l_i - l_f = 1$ have the most probability). As is seen from Fig. 6, at density

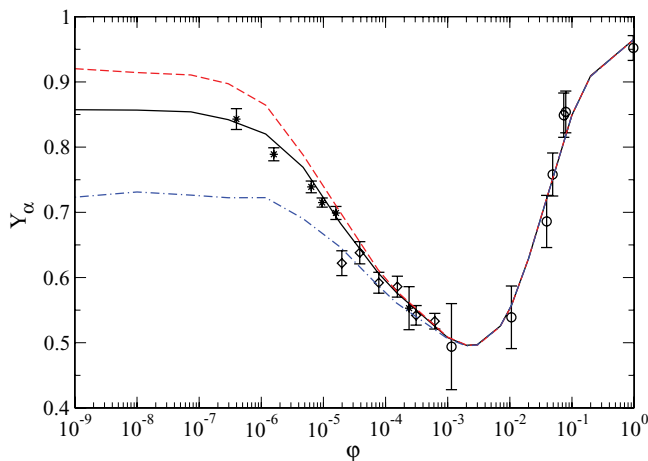


FIG. 6. (Color online) The density dependence of the relative $K\alpha$ -line yield in muonic hydrogen for different variants of the initial l distribution: statistical (dashed line) and modified statistical (solid line for $\alpha_l = 0.08$ and dashed-dotted line for $\alpha_l = 0.2$) distribution. The experimental data are from [37] (asterisks), [38] (diamonds), and [39] (open circles).

$\varphi \lesssim 10^{-7}$ the relative $K\alpha$ -line yield $\sim 85\%$, therefore, about 15% of the radiative transitions ($np \rightarrow 1s$) come from the states of the muonic atom with $n \geq 3$, leading also to the population of muonic hydrogen in the $2s$ state.

It is worthwhile noting that the experimental data [37] could be described assuming the statistical l distribution but for this the initial values of the principal quantum number must satisfy the unrealistic condition $n_i \leq 8$. Contrary to this, the modified statistical distribution with the value $\alpha_l = 0.08$ (solid line) leads as a whole to an excellent agreement between theory and experimental data [37]. At densities higher than $\sim 10^{-3}$ the collisional transitions and mainly Stark mixing become more efficient and the initial l distribution is practically forgotten during the cascade.

The kinetic energy distribution of exotic atoms changes during the cascade and is a more refined probe for the theoretical description of the cascade processes. The present knowledge about the initial kinetic energy distribution is less defined and in the most cascade calculations the fixed values $T_0 \approx (0.5-1)$ eV or the Maxwell distribution with $T_0 = 0.5$ eV [30] are used.

At the lowest densities, as is mentioned above, the initial E distribution is conserved up to the end of the cascade. Hence, the needed information can be obtained from the diffusion experiments. The energy distributions of $(\mu^- p)_{1s}$ have been deduced in diffusion experiments [2,4,5,12] by analyzing the measured time-of-flight spectra data taking into account the scattering processes of $(\mu^- p)_{1s}$ on hydrogen molecules and the surface of the target cylinder. In cascade calculations these processes are not considered and the energy distribution of muonic atoms in the $1s$ state is calculated at the instant of their formation. To exclude, as it is possible, the uncertainties of the rescattering processes (theoretical and experimental) in the analysis of the experimental data we suggest that at the lowest densities these factors can be neglected. It is also important that at the lowest target density the effect of the collisional processes during the cascade can be also neglected.

In the present paper the following two-exponential E distribution (in percent) was used,

$$I = 100 \left(1 - a_0 \exp\left(-\frac{E}{E_1}\right) - (1 - a_0) \exp\left(-\frac{E}{E_2}\right) \right), \quad (20)$$

to describe the integrated energy distribution of muonic hydrogen atoms on arrival at the $1s$ state. The values of the parameters were obtained by fitting the experimental data [12] at the density corresponding to experimental pressure $p_{H_2} = 0.0625$ hPa: $E_1 = 0.469$ eV, $E_2 = 4.822$ eV, and $a_0 = 0.805$.³

The fitted energy distribution (20) was used as an initial one in the cascade model and compared with the result of the cascade calculation. As it is seen from Fig. 7, both distributions are practically indistinguishable, proving the validity of our assumption that at very low density the initial energy distribution is conserved up to the end of the cascade.

³It is possible that the strong difference of the values of E_1 and E_2 is an evidence of two different mechanisms of the exotic atom formation.

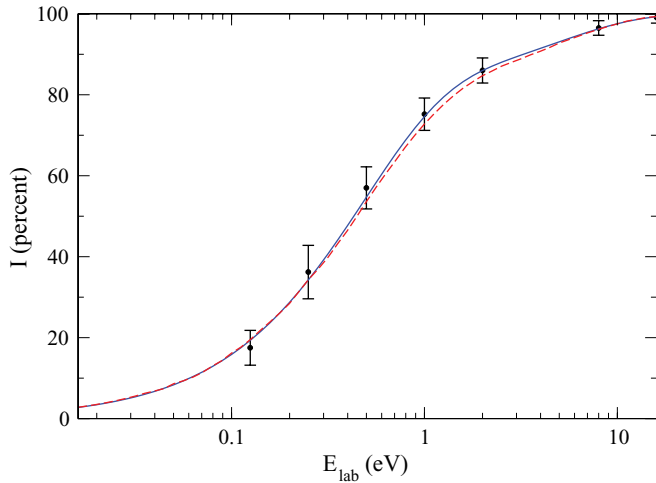


FIG. 7. (Color online) The calculated (dashed line) and fitted experimental (solid line) integrated energy distributions $I(E_{\text{lab}})$ (in percent) of the $(\mu^- p)_{1s}$ at target pressure $p_{\text{H}_2} = 0.0625$ hPa and temperature $T = 300$ K. The experimental data are from [12].

The maximal differences are less than 1% in the energy range of $\sim(1-2)$ eV. The calculated mean kinetic energy, $\bar{E} = 1.25$ eV, is in perfect agreement with the experimental value 1.3 ± 0.8 eV [12].

V. RESULTS OF CASCADE CALCULATIONS

The cascade calculations have been done in the wide density range $\varphi = 10^{-9} - 1$. To obtain good statistics in the cascade calculations the destinies of the 10^7 muonic atoms have been simulated at every value of the density. The initial (n, l, E) distributions defined above were applied in the present cascade calculations at all densities.

A. Energy distributions of muonic hydrogen in $1s$ and $2s$ states at low densities

The energy distribution of muonic hydrogen atoms at the instant of their arrival in the $2s$ state determines their further destiny which also depends on collisional processes in the $2s$ state and target density. In the previous papers [12,30] the assumption that the energy distributions of muonic atoms in the $2s$ and $1s$ states are almost identical was used to estimate the $2s$ state population at kinetic energies below $2p$ threshold. This assumption is valid only at very low target densities $\varphi \lesssim (10^{-7}-10^{-8})$ when the cascade is practically purely radiative and the energy of muonic atom is conserved during the cascade (see Fig. 7).

In fact, there is an essential difference in the population of the $1s$ and $2s$ states, since unlike the $2s$ state the $1s$ state is mainly populated from the $2p$ state (the relative yield of $K\alpha$ is more than $\sim 50\%$ at all densities, as it is seen from Fig. 6). Thus the energy distribution of $(\mu^- p)_{1s}$ is strongly correlated with the energy distribution of $(\mu^- p)_{2p}$ at the instant of radiative $2p \rightarrow 1s$ transition.

In Fig. 8 we present the corresponding integrated kinetic energy distributions of muonic hydrogen on arrival in the $1s$ and $2s$ states calculated at two values of the target densities $\varphi = 7.35 \times 10^{-8}$ and $\varphi = 7.53 \times 10^{-5}$ which correspond (at room

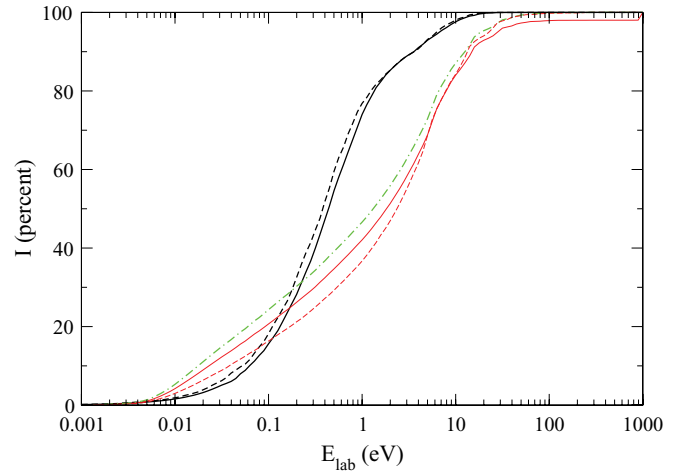


FIG. 8. (Color online) The calculated integrated kinetic energy distributions of the muonic atom on arrival in the $1s$ (solid lines) and $2s$ (dashed lines) states versus laboratory kinetic energy at the gas pressures $p_{\text{H}_2} = 0.0625$ hPa (thick lines) and 64 hPa (thin lines) and $T = 300$ K. The calculated kinetic energy distribution of the $(\mu^- p)_{2p}$ at the instant of the radiative $2p \rightarrow 1s$ transition at $p_{\text{H}_2} = 64$ hPa is shown by a thin dashed-dotted line.

temperature $T = 300$ K) to the pressures $p_{\text{H}_2} = 0.0625$ hPa and 64 hPa, respectively. As it is seen from Fig. 8, the energy distributions of the $1s$ and $2s$ states are rather similar at the density $\varphi = 7.35 \times 10^{-8}$ practically reproducing the initial energy distribution (see also Fig. 7). At higher density these distributions reveal the noticeable distinctions which can be explained by the next reasons.

First, the radiative $2p \rightarrow 1s$ transition contributes in the population of the $1s$ state by about 70% (see Fig. 6) while the radiative transitions from the higher np levels ($n \geq 3$) which are also populating the $2s$ state give less than 30%. As it is seen from Fig. 8, the energy distribution of the $2p$ state before radiative $2p \rightarrow 1s$ transition (thin dashed-dotted line) is less energetic than both the $1s$ and $2s$ states due to deceleration in the elastic scattering of the above lying circular and near circular states. It results in “cooling” the $1s$ state in the energy range $E_{\text{lab}} \lesssim 10$ eV.

Secondly, with increasing density, the contribution of CD becomes more prominent, resulting in a more energetic final E distribution. In particular, Fig. 9 illustrates the effect of the CD at the final stage of the cascade: In the energy distributions of the $1s$ state and $2s$ state one can explicitly see the distinct contributions of the individual Coulomb transitions: $6 \rightarrow 5$, $5 \rightarrow 4$, $6 \rightarrow 4$, and weaker (at this density) from $5 \rightarrow 3$.

It is important to note that the high-energy (~ 0.9 keV) component in the energy distribution of the $1s$ state (see Fig. 9) is about 2% and may be originated only from the $2s \rightarrow 1s$ CD below $2p$ threshold, since above $2p$ threshold the rate of the Stark $2s \rightarrow 2p$ transition about three orders of the magnitude more than the rates of the CD $2s, 2p \rightarrow 1s$ (see Figs. 4 and 5).

B. Arrival population of $2s$ state

The arrival population of the $2s$ state $\epsilon_{2s}^{\text{tot}}$ is defined as the fraction of all formed exotic atoms that during the de-excitation cascade reaches the $2s$ state independently whether

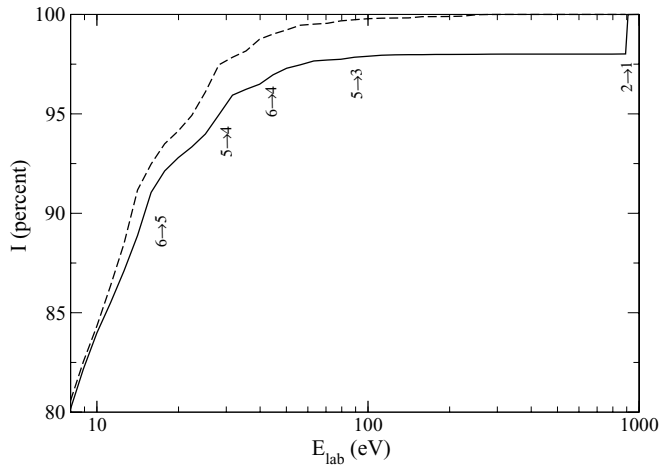


FIG. 9. The calculated integrated kinetic energy distributions of the muonic atom on arrival in the $1s$ (solid line) and $2s$ (dashed line) states versus laboratory kinetic energy at $p_{\text{H}_2} = 64$ hPa and $T = 300$ K.

the kinetic energy of the muonic atom is below or above $2p$ threshold. The atomic cascade at low target densities is mainly dominated by the radiative de-excitation resulting in correlation between the relative yields of K lines and arrival population $\epsilon_{2s}^{\text{tot}}$. The so-called radiative mode of the $2s$ arrival population $\epsilon_{2s}^{\text{rad}}$ is approximately defined [e.g., see [37]] by combining the relative yields Y_i of K lines and the calculated ratios of the radiative transition probabilities $G(np \rightarrow 2s)/G(np \rightarrow 1s)$ for $n = 3$ and $n \geq 4$, respectively]: $\epsilon_{2s}^{\text{rad}} = 0.134Y_\beta + 0.144Y_{>\beta}$ (the numerical coefficients are the branching ratios of the radiative transition probabilities). This relation can be rewritten in a more convenient form,

$$\epsilon_{2s}^{\text{rad}} = 0.134(1 - Y_\alpha) + 0.01Y_{>\beta}, \quad (21)$$

since here the first term gives the main contribution to the value of $\epsilon_{2s}^{\text{rad}}$ and besides the relative yield Y_α is more exactly deduced from the experimental data than both Y_β and $Y_{>\beta}$.

The density dependence of the arrival population $\epsilon_{2s}^{\text{tot}}$ calculated in the present version of the atomic cascade is shown in Fig. 10 in comparison with the population $\epsilon_{2s}^{\text{rad}}$ calculated according to formula (21) with the relative yields Y_i obtained also in the present cascade calculations. At target densities below 2×10^{-4} , the calculated arrival population $\epsilon_{2s}^{\text{tot}}$ is in perfect agreement with the estimation based on formula (21) and in good agreement with the experimental data obtained from the measured x-ray yields [37]. The arrival population $\epsilon_{2s}^{\text{tot}}$ is about 2% in the density range 10^{-9} – 10^{-7} and increases steadily to 6.3% with increasing density to 2×10^{-4} . This behavior is in accordance with the obvious assumption that at low density the $2s$ state is populated by the radiative transitions from the np states with $n \geq 3$ and may be quantitatively explained by the density dependence of the relative $K\alpha$ -line yield. At density below 10^{-7} , the cascade is purely radiative; therefore, the yields of K lines and $2s$ arrival population are determined by the initial conditions and do not have any dependence on density. With the density increasing above 10^{-7} , the Stark transitions result in the enlargement of the np populations at $n \geq 3$, from which radiative $np \rightarrow 2s$

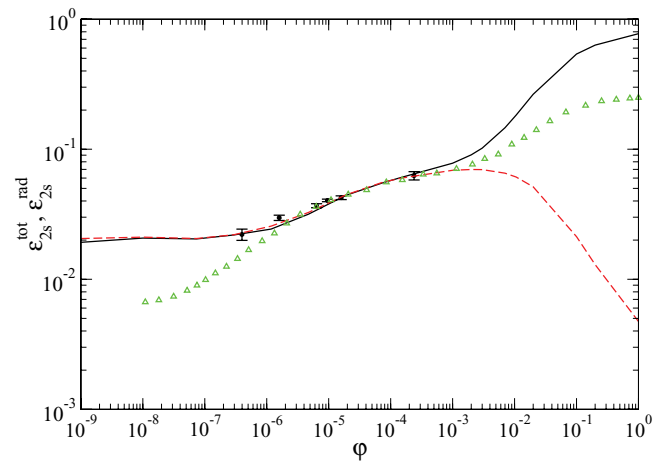


FIG. 10. (Color online) The density dependence of the calculated total arrival population $\epsilon_{2s}^{\text{tot}}$ of the $2s$ state (solid line) in comparison with the values of the $\epsilon_{2s}^{\text{rad}}$ calculated according to formula (21) (dashed line). The triangles correspond to the cascade calculation from [30]. The experimental data (solid circles) are from [37].

transitions populate the $2s$ state (see Fig. 6 of the present paper and Figs. 1 and 2 in [24]).

At densities above 2×10^{-4} , the density dependencies of the $\epsilon_{2s}^{\text{tot}}$ and $\epsilon_{2s}^{\text{rad}}$ are quite different. The population $\epsilon_{2s}^{\text{rad}}$ reaches its maximum value 7% at density $\sim 2 \times 10^{-3}$ and rapidly decreases to 0.5% in liquid hydrogen. This behavior, in general features, corresponds to the density dependence of the relative yields of the K lines and reveals the fact that radiative de-excitation is not a unique process populating the $2s$ state. Indeed, in contrast to the $\epsilon_{2s}^{\text{rad}}$, the $2s$ arrival population $\epsilon_{2s}^{\text{tot}}$ rapidly grows with density increasing and reaches about 77% at liquid-hydrogen density ($\phi = 1$) exceeding the statistical weight of the $2s$ state more than three times. This behavior has a simple explanation: at density above 2×10^{-4} , the role of the Stark mixing gradually grows also for the $n = 2$ state of the muonic atom with density increasing until at $\phi \sim 10^{-2}$ the rate of the Stark $2p \rightarrow 2s$ transition is compared with the rate of the radiative $2p \rightarrow 1s$ transition and becomes about two orders of magnitude more at liquid-hydrogen density ($\phi = 1$) (see Fig. 5). Thus, at density above 10^{-2} the $2s$ state is mainly populated due to the always open Stark $2p \rightarrow 2s$ transition.

In the density range $\sim 10^{-5}$ – 10^{-3} , the density dependence of the $\epsilon_{2s}^{\text{tot}}$ calculated in the present paper is in good agreement with the results, obtained earlier in the paper [30]. However, there are essential differences at densities both below and above this range. The arrival population of the $2s$ state, calculated in the paper [30] changes from 0.8% at density 10^{-8} to 25% in liquid hydrogen, in contrast to our results (from 2% to 77%) in the same density range. It is possible that the origin of the discrepancy at the lowest density is simply explained by using the statistical l distribution in [30]. At the same time, it is difficult to explain the significant disagreement at higher densities. Moreover, according to [30], at liquid-hydrogen density the calculated arrival $2s$ population is significantly less (~ 2.5 times) than the population of the metastable $2s$ state.

C. Metastable $2s$ fraction: population, lifetime, and yield of high-energy component of $(\mu^- p)_{1s}$

The further destiny of the initially formed muonic hydrogen in the $2s$ state depends on its kinetic energy distribution. The fraction with kinetic energy above $2p$ threshold changes in the collisions due to deceleration in the elastic $2s$ - $2s$ scattering and $2s \rightarrow 2p$ Stark transition (above the $2p$ threshold) followed by the fast radiative $2p \rightarrow 1s$ transition. As a result only part of all the created $(\mu^- p)_{2s}$ survives at the kinetic energy below $2p$ threshold.

The population $\epsilon_{2s}^{\text{long}}$ of the *metastable* (or *long-lived*) $2s$ state is defined as the fraction of all created $(\mu^- p)_{2s}$ with kinetic energies below the $2p$ threshold. This fraction is the metastable fraction of the $2s$ state as the Stark $2s \rightarrow 2p$ transition is energetically forbidden and the rate of the two-photon transition to the $1s$ state is negligibly small as compared with the rate of muon decay, $\lambda_\mu = 4.55 \times 10^5 \text{ s}^{-1}$. The delayed $K\alpha$ line induced during the collisions [40–42] can also occur but has never been observed [43,44].

The density dependence of the population $\epsilon_{2s}^{\text{long}}$ calculated in the present version of the atomic cascade is shown in Fig. 11 for the two variants of the initial l distribution: statistical ($\alpha_l = 0$) and modified statistical ($\alpha_l = 0.08$) distribution. In general features the density dependencies of the $\epsilon_{2s}^{\text{long}}$ calculated for these variants are similar. At densities below 10^{-4} , the metastable fraction calculated with the statistical l distribution is less than the one obtained with the modified statistical l distribution and changes from 0.6% to 2.3% while density increases from 10^{-8} to 10^{-4} , respectively. According to our study, the metastable fraction calculated with the modified statistical l distribution ($\alpha_l = 0.08$) is about 1% below 10^{-7} and slowly increases in the density range (10^{-7} – 10^{-4}) to 2.4%. It is worthwhile noting that density dependence of the $\epsilon_{2s}^{\text{long}}$ calculated in the present study with the statistical l distribution

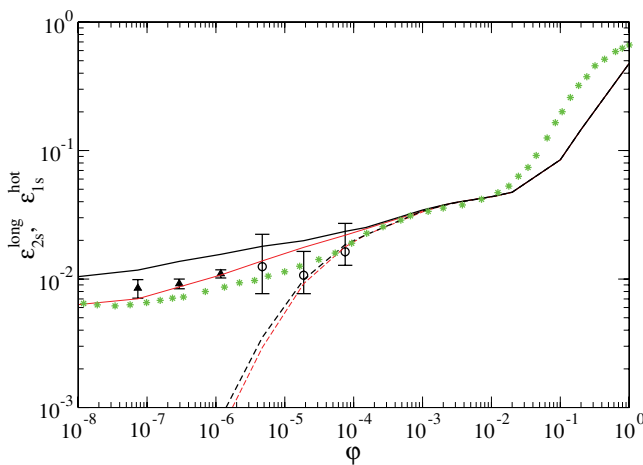


FIG. 11. (Color online) *Ab initio* cascade calculation of the population $\epsilon_{2s}^{\text{long}}$ (solid lines) and the yield $\epsilon_{1s}^{\text{hot}}$ (dashed lines) of the $(\mu p)_{1s}$ (0.9 keV) (thick lines for $\alpha_l = 0.08$ and thin lines for $\alpha_l = 0$). The asterisks correspond to the cascade calculations of the $\epsilon_{2s}^{\text{long}}$ in [30]. The experimental values of $\epsilon_{2s}^{\text{long}}$ are from indirect determination [12] (black triangles), and direct determination [13] (open circles).

is similar to the one obtained earlier in [30] only at densities below 10^{-4} .

Above 10^{-4} , the calculated metastable fraction does not depend on the initial l distribution due to more efficient Stark mixing in the states with $n > 3$ (the same picture was observed in the relative $K\alpha$ -line yield in Fig. 6). At densities above 10^{-2} , the $\epsilon_{2s}^{\text{long}}$ grows faster reaching 47% in liquid hydrogen.⁴ This behavior and growth of the metastable fraction at density above 10^{-2} is a consequence of the dominant role of the elastic scattering ($2p \rightarrow 2p$, $2s \rightarrow 2s$) and Stark ($2p \rightarrow 2s$) transition over the radiative $2p \rightarrow 1s$ transition (as in the density dependence of the $\epsilon_{2s}^{\text{tot}}$ discussed above).

As seen from Fig. 11, at densities below 10^{-4} , the calculations with the modified l distribution predict a higher population $\epsilon_{2s}^{\text{long}}$ as compared with the direct [13] (open circles) and indirect [12] (solid triangles) determinations of the population derived from the experimental data analysis (for details, see [12,13]). The observed difference at the lowest density ($\varphi = 7.35 \times 10^{-8}$) can be simply explained by the underestimation in [12,30] of the $\epsilon_{2s}^{\text{tot}}$ value at this density. Using the value of $\epsilon_{2s}^{\text{tot}} \cong 2\%$ at this density (see Fig. 10) one can correct the experimental value of $\epsilon_{2s}^{\text{long}}$ and obtain $\epsilon_{2s}^{\text{long}} \cong 1.2\%$ which is in perfect agreement with our result. According to our analysis there are no reasons leading to the decreasing of the $\epsilon_{2s}^{\text{long}}$ while density is increasing. Hence, the general tendency of the $\epsilon_{2s}^{\text{long}}$ increasing with density must also be revealed in the experimental data at higher densities.

After the formation of $(\mu^- p)_{2s}$ atoms at energy below the $2p$ threshold their kinetic energy distribution $F_{2s}(E; \varphi)$ changes because of elastic $2s \rightarrow 2s$ scattering until muon decay or Coulomb $2s \rightarrow 1s$ de-excitation occurs. In the last process (1) the transition energy (1.898 keV) is shared between the $(\mu^- p)_{1s}$ and a proton from the hydrogen molecule. The yield of the $(\mu^- p)_{1s}$ with kinetic energy about 0.9 keV is defined by the integral,

$$\epsilon_{1s}^{\text{hot}}(\varphi) = \int_0^{E_{\text{thr}}} F_{2s}(E; \varphi) \frac{\lambda_{2s}^{\text{CD}}(E; \varphi)}{\lambda_\mu + \lambda_{2s}^{\text{CD}}(E; \varphi)} dE, \quad (22)$$

where $\lambda_{2s}^{\text{CD}}(E; \varphi)$ is the rate of the Coulomb $2s \rightarrow 1s$ de-excitation and the energy distribution $F_{2s}(E; \varphi)$ satisfies the next condition:

$$\int_0^{E_{\text{thr}}} F_{2s}(E; \varphi) dE = \epsilon_{2s}^{\text{long}}(\varphi). \quad (23)$$

The yield $\epsilon_{1s}^{\text{hot}}$ can be also deduced from the kinetic energy distribution of $(\mu p)_{1s}$ as the fraction of all $(\mu p)_{1s}$ formed with kinetic energy about 0.9 keV. Considering in (22) the limits $\lambda_\mu \gg \bar{\lambda}_{2s}^{\text{CD}}(\varphi)$ and $\lambda_\mu \ll \bar{\lambda}_{2s}^{\text{CD}}(\varphi)$ we, respectively, obtain

$$\epsilon_{1s}^{\text{hot}}(\varphi) \approx \bar{\lambda}_{2s}^{\text{CD}}(\varphi) / \lambda_\mu, \quad (24)$$

and

$$\epsilon_{1s}^{\text{hot}}(\varphi) \approx \epsilon_{2s}^{\text{long}}(\varphi), \quad (25)$$

⁴Our calculations do not confirm the greater increasing of the population up to 65% at LHD predicted in [30].

where

$$\bar{\lambda}_{2s}^{\text{CD}}(\varphi) = \int_0^{E_{\text{thr}}} F_{2s}(E; \varphi) \lambda_{2s}^{\text{CD}}(E; \varphi) dE \quad (26)$$

is the mean rate of the $2s \rightarrow 1s$ CD at given density. According to our estimations (see Fig. 3), the condition $\lambda_{\mu} \gg \bar{\lambda}_{2s}^{\text{CD}}(\varphi)$ is valid at density $\lesssim 10^{-6}$ while the other condition $\lambda_{\mu} \ll \bar{\lambda}_{2s}^{\text{CD}}(\varphi)$ is fulfilled at density above $\sim 10^{-4}$. At low density the mean rate $\bar{\lambda}_{2s}^{\text{CD}}(\varphi)$ has a nonlinear dependence on density until at $\varphi \approx 10^{-5}$ the mean rate of the elastic $2s \rightarrow 2s$ scattering (below the $2p$ threshold) becomes much more than the muon decay rate. Above this density, the energy distribution $F_{2s}(E; \varphi)$ is almost independent of density and $\bar{\lambda}_{2s}^{\text{CD}}(\varphi)$ is proportional to φ .

In the intermediate range the yield $\epsilon_{1s}^{\text{hot}}(\varphi)$ can be evaluated applying in Eq. (22) the mean value theorem for integral:

$$\epsilon_{1s}^{\text{hot}}(\varphi) \approx \epsilon_{2s}^{\text{long}}(\varphi) \frac{\lambda_{2s}^{\text{CD}}(E^*; \varphi)}{\lambda_{\mu} + \lambda_{2s}^{\text{CD}}(E^*; \varphi)}. \quad (27)$$

However, this formula gives rather a rough estimation of the $\epsilon_{1s}^{\text{hot}}(\varphi)$ since the $\lambda_{2s}^{\text{CD}}(E; \varphi)$ changes about three orders of the magnitude (see Fig. 3) in the integration range. Comparing Eqs. (25) and (27), one can conclude that the approximation (27) has a sense at the condition $\lambda_{2s}^{\text{CD}}(E^*; \varphi) \gg \lambda_{\mu}$. Note that $\epsilon_{1s}^{\text{hot}}(\varphi)$ and $\lambda_{2s}^{\text{CD}}(E^*; \varphi)$ are correlated with each other in accord with (27) and cannot be used as free fit parameters (see [13]). Moreover, since

$$\lambda_{2s}^{\text{CD}}(E^*; \varphi) \neq \bar{\lambda}_{2s}^{\text{CD}}(\varphi),$$

then the $2s$ quench time,

$$\tau_{2s}^{\text{quench}} = 1/\bar{\lambda}_{2s}^{\text{CD}}(\varphi) \neq 1/\lambda_{2s}^{\text{CD}}(E^*; \varphi).$$

It is possible that these remarks can explain the observed discrepancies in Fig. 11 between the calculated and the so-called direct determination in Ref. [13] values of the $\epsilon_{2s}^{\text{long}}$.

The general features discussed above of the $\epsilon_{1s}^{\text{hot}}(\varphi)$ are confirmed by the detailed cascade calculations in the wide density range from 10^{-8} up to 1. The calculated yield of the hot (0.9 keV) fraction of $(\mu p)_{1s}$, $\epsilon_{1s}^{\text{hot}}(\varphi)$, is shown in Fig. 11. According to our study, this fraction is formed due to the direct CD process (1).

At densities below 10^{-4} the yield $\epsilon_{1s}^{\text{hot}}$ reveals a *quite different* density dependence as compared with the one of the $\epsilon_{2s}^{\text{long}}$, since its value essentially depends on the kinetic energy distribution of $(\mu p)_{2s}$ below the $2p$ threshold and the competition between muon decay and CD rates. In the density range (10^{-8} – 10^{-6}) the yield of the hot fraction in accordance with Eq. (24) is less than $\sim 0.07\%$ and grows rapidly up to $\sim 2\%$ while density is increasing up to $\sim 10^{-4}$. Such density dependence of the $\epsilon_{1s}^{\text{hot}}$ is in perfect agreement with the experimental data [12,13], in which the pronounced peak in time-of-flight $(\mu p)_{1s}$ spectra measured at pressure $p_{\text{H}_2} = 64$ hPa was observed. According to [12,13] this peak was less pronounced at lower pressure $p_{\text{H}_2} = 16$ hPa and practically disappears at $p_{\text{H}_2} = 4$ hPa. Above 10^{-3} , the values of the $\epsilon_{1s}^{\text{hot}}$ and $\epsilon_{2s}^{\text{long}}$ are practically equal to each other in accord with (25) as it is demonstrated in Fig. 10.

Such a behavior can be explained by the growth of the thermal fraction in the kinetic energy distribution of the

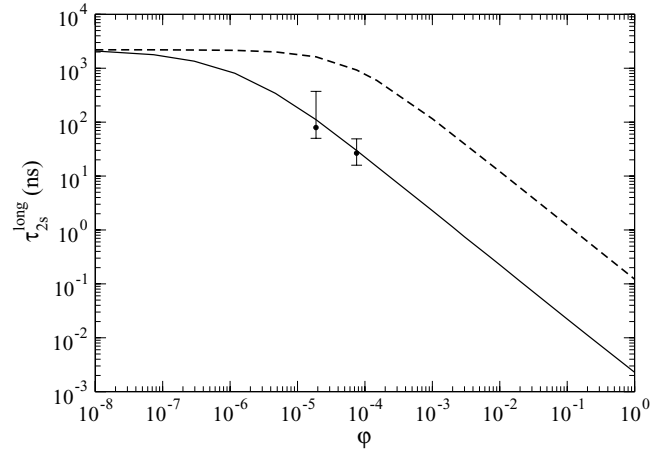


FIG. 12. The density dependence of the lifetime τ_{2s}^{long} calculated with the extended basis set with $n_{\text{max}} \rightarrow \infty$ (solid line) is shown in comparison with the one in which only the closed $2p$ state is added to the basis (dashed line). The experimental values from [13].

$(\mu p)_{2s}$ atoms due to elastic $2s \rightarrow 2s$ scattering below the $2p$ threshold. At very low densities (below 10^{-7}) this fraction in the kinetic energy distribution of the $(\mu p)_{2s}$ is negligibly small and the yield of the hot $(\mu p)_{1s}$ is practically equal to zero. At higher densities (above $\sim 10^{-6}$) it sharply increases with density and at density above $\sim 10^{-3}$ all $(\mu p)_{2s}$ atoms (below the $2p$ threshold) are quenched by the direct $2s \rightarrow 1s$ CD. According to our study, we also predict the yield of the 0.9 keV $(\mu p)_{1s}$ atoms and the possible yield of the protons with kinetic energy ~ 1 keV about $\sim 47\%$ in liquid hydrogen.

The density dependence of the lifetime of the metastable fraction,

$$\tau_{2s}^{\text{long}}(\varphi) = \frac{1}{\lambda_{\mu} + \bar{\lambda}_{2s}^{\text{CD}}(\varphi)},$$

calculated with the extended basis set with $n_{\text{max}} \rightarrow \infty$ (solid line) and with the basis including only the closed $2p$ state (dashed line) is shown in Fig. 12. At densities below 10^{-7} , the lifetime of the metastable $2s$ state is mainly determined by the muon lifetime. At the density range (10^{-7} – 10^{-5}) we observe the competition between the muon decay and the nonradiative quenching of the metastable $2s$ state due to the direct CD $2s \rightarrow 1s$. Above (10^{-5} – 10^{-4}) the quenching of the long-lived $2s$ state is entirely determined by the CD process. The perfect agreement of the calculations (with the extended basis set) with the experimental data [13] may be considered as the confirmation of the dominant role CD in the nonradiative quenching of the metastable $2s$ state. The calculated value $\bar{\lambda}_{2s}^{\text{CD}}(\text{LHD}) = 4.38 \times 10^{11} \text{ s}^{-1}$ is in excellent agreement with the experimental value $\lambda_{2s}^{\text{quench}} = 4.4_{-1.8}^{+2.1} \times 10^{11} \text{ s}^{-1}$ [13].

VI. CONCLUSION

The differential and total cross sections of the $(\mu p)_{nl} + H \rightarrow (\mu p)_{n'l'} + H$ scattering processes—elastic, Stark, and Coulomb de-excitation—have been calculated for the initial values of the principal quantum numbers $n = 2$ –8 and kinetic energies needed in the detailed study of atomic cascade kinetics. The calculations of the cross sections have been

performed in a fully quantum mechanical framework using the close-coupling approach *including the closed channels*. To integrate the system of CCA equations including closed channels, we have developed a new propagation matrix method which does not include the calculation of the wave functions themselves (exponentially growing in closed channels) but uses only the ratio of their values at neighboring points. The energy Lamb shifts between ns and np states have been explicitly taken into account in the scattering problem. The convergence of the cross sections to the extension of the basis set have been studied, so the threshold behavior of the cross sections is treated correctly and the corresponding cross sections of the elastic scattering, Stark transitions and Coulomb de-excitation are calculated reliably both above and below ns - np thresholds. In particular, the cross sections of the elastic scattering ($2s$ - $2s$) and Coulomb de-excitation ($2s$ - $1s$) which are very important for the problem of metastable $2s$ state in muonic hydrogen have been calculated below the $2p$ threshold.

The atomic cascade kinetics has been investigated within the new version of the extended standard cascade model taking into account both the new results for collisional processes and the initial distributions in the quantum numbers (n , l) and the kinetic energy. In the wide density range ($\varphi = 10^{-9} - 1$) a number of the different characteristics of the atomic cascade have been calculated: the relative $K\alpha$ -line yield, the arrival population $\epsilon_{2s}^{\text{tot}}$, the population of the metastable fraction $\epsilon_{2s}^{\text{long}}$, the yield $\epsilon_{1s}^{\text{hot}}$ of the $(\mu^- p)_{1s}$ (0.9 keV), and the lifetime τ_{2s}^{long} . The calculations of the kinetic energy distributions of muonic hydrogen on arrival in the $1s$ and $2s$ states are also presented at different densities. The results of the present cascade calculations can be summarized as follows.

The calculated relative $K\alpha$ -line yield is in excellent agreement with the data [37–39]. The $K\alpha$ -line yield measured in [37] can be reproduced if the modified statistical l distribution is applied at the beginning of the cascade. The calculated kinetic energy distributions of muonic hydrogen on arrival in the $1s$ and $2s$ states reveal their noticeable distinctions which is mainly explained by the contribution of the radiative transition $2p \rightarrow 1s$ on the formation of the $1s$ state.

Ab initio cascade calculations of the $2s$ arrival population and the population of the metastable fraction $\epsilon_{2s}^{\text{long}}$ allowed us to obtain their density dependence more realistically than earlier in [30]. It is shown that at density above 10^{-3} the $2s$ state is mainly formed due to Stark transition $2p \rightarrow 2s$. The calculated $2s$ arrival population is in perfect agreement with the experimental data obtained from x-ray yields [37] and changes from 2% up to 77% at the density range $\varphi = 10^{-8} - 1$. According to our present study, the $\epsilon_{2s}^{\text{long}}$ increases from 1% up to 47% while density changes from 10^{-8} up to LHD. The obtained results for $\epsilon_{2s}^{\text{long}}$ with the modified initial l distribution are in fair agreement with the ones derived from the experimental data analysis [12,13] at low densities. The possible reasons for these distinctions are discussed.

Ab initio quantitative description of the yield $(\mu^- p)_{1s}$ (0.9 keV) and the lifetime τ_{2s}^{long} are obtained. At densities below 10^{-4} , the density dependence of the $(\mu^- p)_{1s}$ (0.9 keV) is in very good agreement with the observations deduced from

the experimental data [12,13]. It is shown that the CD process results in the quench of all metastable fraction at densities above 10^{-3} . The results of the present consideration allow us to confirm our previous suggestion that the direct Coulomb de-excitation is the *dominant quenching mechanism* of the long-lived $2s$ fraction leading to the formation of $(\mu^- p)_{1s}$ (0.9 keV) and perfect agreement of the calculated and experimental values of its lifetime. It will be very interesting to obtain the experimental confirmation of our predictions on the density dependence of the yield of the hot component $(\mu p)_{1s}$ with kinetic energy ~ 0.9 keV or the yield of the protons with kinetic energy about 1 keV.

We conclude that the present study demonstrates the overall reliability of the theoretical description of collisional processes and good understanding of muonic hydrogen cascade kinetics. The obtained results serve a good foundation for applying the current theory of the cascade processes to the study of hadronic hydrogen atoms.

ACKNOWLEDGMENTS

The authors thank L. Simons and G. Korenman for permanent interest in our studies and fruitful discussions, T. Jensen for the fruitful cooperation in the development of the new version of the cascade code, and R. Pohl for e-mail correspondence regarding some questions under consideration. This work was supported by Russian Foundation for Basic Research (Grant No. 10-02-01096).

APPENDIX

The system equations for the coupling-channel method is a system of N -coupled second-order differential equations without the first derivatives. This system has N linearly independent solutions $\Psi_j^{(i)}(R)$ (i is the number of the solution, j is the channel index) which are regular at $R = 0$. Let us write this system in matrix form ($\{\Psi(R)\}_{ij} = \Psi_j^{(i)}(R)$):

$$\Psi''(R) = V(R)\Psi(R), \quad (\text{A1})$$

where

$$\{V(R)\}_{ij} \equiv 2m[W_{ij}(R) + \delta_{ij}(W_i^{cf}(R) - (E - \epsilon_i))],$$

$W_{ij}(R)$ are the elements of the potential matrix, and $W_i^{cf}(R)$ is the centrifugal term. The standard way of solving such a problem is the following: one finds N independent solutions of the system (A1) which are regular at $R = 0$ and then matches them at sufficiently large $R = R_0$ with the asymptotic solutions corresponding to the scattering problem. From this matching procedure one obtains S or K matrix.

The difficulties due to the exponential growth of independent solutions can appear in the numerical solution of coupled-channel Eqs. (A1). In particular, the exponentially increasing functions arise in closed channels and in channels corresponding to the unstable states of the subsystem with finite width, in problems with complex interactions and also in the case when the off-diagonal elements of matrix V are much more than its diagonal elements.

However, the determination of the S or K matrix requires only logarithmic derivatives of wave functions at the point of

matching or the ratio of the functions in the two neighboring points. Such quantities are limited and may be calculated even in case of exponentially growing functions without any numerical problems.

Such an object is a matrix U constructed from the N linearly independent solutions regular at zero and their first derivatives:

$$U(R) = \Psi(R)[\Psi'(R)]^{-1}. \quad (\text{A2})$$

The matrix U satisfies the nonlinear differential equation of the first order:

$$U' = 1 + UVU. \quad (\text{A3})$$

The solution of this equation with the boundary condition at zero $U(0) = 0$ is a suitable object to determine the K matrix by its matching with known asymptotic solution at $R = R_0$. It is obvious that the matrix $U(R)$ is symmetric in the case of symmetric potential W and bounded except for a finite number of points where the matrix of independent solutions $\Psi(R)$ has no inverse. Note that in the case of a one-channel problem the asymptotic solution at $R \rightarrow \infty$ is $U(R) = p^{-1} \tan(pR + L\pi/2 + \delta)$ where p is the wave number and δ is the scattering phase shift.

In the numerical realization of this approach it is convenient to use the discrete analog of matrix U —the matrix $D(R) = \Psi(R)[\Psi(R+h)]^{-1}$ —which can be called a propagation matrix [45]. Here h is the constant integration step. The two-point numerical scheme for the calculation of D is easily deduced from any three-point scheme for solving the initial equations of second order. The most widely used Numerov scheme has a form:

$$\tilde{\Psi}(R+h) = \tilde{\Psi}(R-h) + 2\tilde{\Psi}(R) + \tilde{V}(R)\tilde{\Psi}(R), \quad (\text{A4})$$

where

$$\tilde{V} = Vh^2[1 - Vh^2/12]^{-1},$$

and

$$\tilde{\Psi}(R) = \Psi(R) - h^2/12\Psi''(R)$$

is the so-called Numerov representation for $\Psi(R)$. Multiplying Eq. (A4) right by $[\tilde{\Psi}(R)]^{-1}$ one gets the two-point iteration scheme for the propagation matrix $\tilde{D}(R) = \tilde{\Psi}(R)[\tilde{\Psi}(R+h)]^{-1}$ constructed from the Numerov solutions:

$$\tilde{D}(R) = \{2 - \tilde{D}(R-h) + \tilde{V}(R)\}^{-1}. \quad (\text{A5})$$

Regularity at the origin for $\Psi(R)$ [and hence for $\tilde{\Psi}(R)$] implies the initial condition $\tilde{D}(0) = 0$ for iterations (A5), propagation matrix \tilde{D} being symmetric at every step.

Now we obtain the matching conditions for matrix $U = \Psi[\Psi']^{-1}$ in the presence of the closed or nonstationary channels. If all channels are open one has the usual boundary conditions at the matching point R_0 :

$$U(R_0) = \Phi(R_0)[\Phi'(R_0)]^{-1}, \quad (\text{A6})$$

where $\Phi(R)$ is the matrix of the asymptotic physical solutions expressed in terms of the K matrix:

$$\Phi(R) = j(R) - y(R)K. \quad (\text{A7})$$

Here $j(R)$ and $y(R)$ are the diagonal matrices consisting of Ricatti-Bessel functions,

$$\begin{aligned} \{j(R)\}_{ij} &= \delta_{ij} j_{L_i}(p_i R), \\ \{y(R)\}_{ij} &= \delta_{ij} y_{L_i}(p_i R), \end{aligned}$$

L_i is the orbital angular momentum, and $p_i = \sqrt{2m(E - \varepsilon_i)}/\hbar$ is the wave number of channel i .

If any of the channels are closed [$(E - \varepsilon_i) < 0$] or nonstationary [$\text{Im}(E - \varepsilon_i) > 0$] ones (for brevity we call all such channels closed ones) then the matching algorithm must be changed. The wave numbers p_i in such closed channels take imaginary or complex values. Let us divide all N channels into the set of open channels α with dimension M and the set of closed channels β with dimension $N - M$. Unlike the case of open channels (A6), the matrices $\Phi(R)$ and $\Phi'(R)$ have no inverse, so we write the matching condition at $R = R_0$ in the form,

$$U(R_0)\Phi'(R_0) = \Phi(R_0). \quad (\text{A8})$$

Since the physical wave function of a closed channel decreases exponentially at $R \rightarrow \infty$, there are no solutions corresponding to incident wave in the closed channels. Therefore, the matrix of asymptotic solutions Φ (and similarly Φ') is divided into four sub-matrices, two of which (corresponding to the incident wave in the closed channel) can be set equal to zero:

$$\Phi(R) = \begin{pmatrix} \Phi_\alpha(R) & 0 \\ \Phi_\beta(R) & 0 \end{pmatrix}. \quad (\text{A9})$$

Here the $(M \times M)$ matrix $\Phi_\alpha(R)$ is the matrix of asymptotic solutions in the space of open channels, which has the standard form (A7). The rectangular $((N - M) \times M)$ matrix $\Phi_\beta(R)$ contains a combination of damped asymptotic solutions:

$$\Phi_\beta(R) = h^{(-)}(R)C, \quad (\text{A10})$$

where $h^{(-)}(R)$ is the diagonal $((N - M) \times (N - M))$ matrix composed of damped Ricatti-Hankel functions $\{h^{(-)}(R)\}_{ij} = \delta_{ij} h_{L_i}^{(-)}(p_i R)$, and C is the rectangular $((N - M) \times M)$ matrix corresponding to the transitions from open channels to nonstationary or closed ones.

In accordance with the division of channels into α and β sets, the matrix of linearly independent solutions U at $R = R_0$ is also divided into four submatrices:

$$U(R_0) = \begin{pmatrix} U_{\alpha\alpha} & U_{\alpha\beta} \\ U_{\beta\alpha} & U_{\beta\beta} \end{pmatrix}. \quad (\text{A11})$$

Now Eq. (A8) can be written as a system of two matrix equations:

$$\begin{aligned} U_{\alpha\alpha}\Phi'_\alpha + U_{\alpha\beta}\Phi'_\beta &= \Phi_\alpha, \\ U_{\beta\alpha}\Phi'_\alpha + U_{\beta\beta}\Phi'_\beta &= \Phi_\beta. \end{aligned} \quad (\text{A12})$$

From these two matrix equations one can determine the unknown matrices K and C . The matrix C has no physical meaning, therefore we exclude it by means of the second equation in (A12). The form of Φ_β in Eq. (A10) implies the following relation:

$$\Phi_\beta = h^{(-)}[(h^{(-)})']^{-1}\Phi'_\beta,$$

so

$$\Phi'_\beta = [h^{(-)}[(h^{(-)})']^{-1} - U_{\beta\beta}]^{-1} U_{\beta\alpha} \Phi'_\alpha. \quad (\text{A13})$$

Substituting Eq. (A13) into the first equation in (A12) one finally obtains the matching condition:

$$U_{\alpha\alpha} \Phi'_\alpha + U_{\alpha\beta} [h^{(-)}[(h^{(-)})']^{-1} - U_{\beta\beta}]^{-1} U_{\beta\alpha} \Phi'_\alpha = \Phi_\alpha, \quad (\text{A14})$$

which can be written in the form,

$$\hat{U}_{\alpha\alpha} \Phi'_\alpha = \Phi_\alpha, \quad \text{or} \quad \hat{U}_{\alpha\alpha} = \Phi_\alpha [\Phi'_\alpha]^{-1}, \quad (\text{A15})$$

where

$$\hat{U}_{\alpha\alpha} = U_{\alpha\alpha} + \underbrace{U_{\alpha\beta} [h^{(-)}[(h^{(-)})']^{-1} - U_{\beta\beta}]^{-1} U_{\beta\alpha}}_{\Delta U_{\alpha\alpha}}. \quad (\text{A16})$$

Thus, the form of matching condition in the presence of the closed and nonstationary channel remains the same as in the case of open channels [cf. (A6) and (A15)], but the matrix of the solutions in the space of the open channels $U_{\alpha\alpha}$ is modified by adding the term $\Delta U_{\alpha\alpha}$, which provides the damping of physical solutions in the closed (nonstationary) channels.

For the propagation matrix D (or \tilde{D} for Numerov scheme) one can obtain the matching condition similar to (A15)–(A16) which includes matrices $\Phi_\alpha(R_0)[\Phi_\alpha(R_0 + h)]^{-1}$ instead of $\Phi_\alpha[\Phi'_\alpha]^{-1}$. Note that the effect of this additive $\Delta U_{\alpha\alpha}$ (or the corresponding correction for the propagator matrix D) on the physical elements K matrix is usually negligible (except for the case of the very weakly closed channels), and in most cases one can use the matching only in the space of open channels without considering this correction.

-
- [1] J. F. Crawford, M. Daum, R. Frosch, B. Jost, P. R. Kettle, R. M. Marshall, B. K. Wright, and K. O. H. Ziock, *Phys. Rev. D* **43**, 46 (1991).
- [2] D. J. Abbott *et al.*, *Phys. Rev. A* **55**, 214 (1997).
- [3] A. Badertscher *et al.*, *Europhys. Lett.* **54**, 313 (2001).
- [4] F. Kottman *et al.*, *Hyperf. Interact.* **119**, 3 (1999); F. Kottman *et al.*, *Hyperf. Interact.* **138**, 55 (2001).
- [5] R. Pohl *et al.*, *Hyperf. Interact.* **138**, 35 (2001).
- [6] H.-Ch. Schröder *et al.*, *Eur. Phys. J. C* **21**, 473 (2001).
- [7] D. Gotta *et al.*, *Lect. Notes Phys.* **745**, 165 (2008).
- [8] D. S. Covita *et al.*, *Phys. Rev. Lett.* **102**, 023401 (2009).
- [9] D. Gotta, *Prog. Part. Nucl. Phys.* **52**, 133 (2004).
- [10] E. Borie, *Phys. Rev. A* **71**, 032508 (2005).
- [11] R. Pohl *et al.*, *Nature (London)* **466**, 213 (2010).
- [12] R. Pohl, Ph.D. thesis, ETH Zurich No. 14096, 2001.
- [13] R. Pohl *et al.*, *Phys. Rev. Lett.* **97**, 193402 (2006).
- [14] P. Froelich and A. Flores-Riveros, *Phys. Rev. Lett.* **70**, 1595 (1993).
- [15] S. Jonsell, J. Wallenius, and P. Froelich, *Phys. Rev. A* **59**, 3440 (1999).
- [16] J.W. allenius, S. Jonsell, Y. Kino, and P. Froelich, *Hyperf. Interact.* **138**, 285 (2001).
- [17] V. N. Pomerantsev and V. P. Popov, *JETP Lett.* **83**, 331 (2006).
- [18] V. P. Popov and V. N. Pomerantsev, e-print [arXiv:0809.0742](https://arxiv.org/abs/0809.0742).
- [19] G. Ya. Korenman, V. N. Pomerantsev, and V. P. Popov, *JETP Lett.* **81**, 543 (2005).
- [20] V. N. Pomerantsev and V. P. Popov, *Phys. Rev. A* **73**, 040501(R) (2006).
- [21] V. P. Popov and V. N. Pomerantsev, e-print [arXiv:nucl-th/0512107](https://arxiv.org/abs/nucl-th/0512107).
- [22] V. P. Popov and V. N. Pomerantsev, e-print [arXiv:0712.3111](https://arxiv.org/abs/0712.3111).
- [23] V. P. Popov and V. N. Pomerantsev, *Hyperf. Interact.* **138**, 109 (2001).
- [24] T. S. Jensen, V. P. Popov, and V. P. Pomerantsev, e-print [arXiv:0712.3010](https://arxiv.org/abs/0712.3010).
- [25] S. M. Wang, *Phys. Rev.* **31**, 579 (1928).
- [26] M. Leon and H. A. Bethe, *Phys. Rev.* **127**, 636 (1962).
- [27] E. Borie and M. Leon, *Phys. Rev. A* **21**, 1460 (1980).
- [28] T. P. Terada and R. S. Hayano, *Phys. Rev. C* **55**, 73 (1997).
- [29] V. E. Markushin, *Phys. Rev. A* **50**, 1137 (1994).
- [30] T. S. Jensen and V. E. Markushin, *Eur. Phys. J. D* **21**, 271 (2002).
- [31] T. S. Jensen and V. E. Markushin, *Eur. Phys. J. D* **19**, 157 (2002).
- [32] L. Bracci and G. Fiorentini, *Nuovo Cimento A* **43**, 9 (1978).
- [33] G. Ya. Korenman and V. P. Popov, *AIP Conf. Proc.* **181**, 145 (1988).
- [34] G. Ya. Korenman, V. P. Popov, and G. A. Fesenko, *Muon Catal. Fusion* **7**, 179 (1992).
- [35] J. S. Cohen, *Phys. Rev. A* **59**, 4300 (1999).
- [36] J. S. Cohen, *Rep. Prog. Phys.* **67**, 1769 (2004).
- [37] H. Anderhub *et al.*, *Phys. Lett. B* **143**, 65 (1984).
- [38] N. Bregant *et al.*, *Phys. Lett. A* **241**, 344 (1998).
- [39] B. Lauss *et al.*, *Phys. Rev. Lett.* **80**, 3041 (1998).
- [40] R. O. Mueller *et al.*, *Phys. Rev. A* **11**, 1175 (1975).
- [41] J. S. Cohen and J. N. Bardsley, *Phys. Rev. A* **23**, 46 (1981).
- [42] L. I. Men'shikov and L. I. Ponomarev, *Z. Phys. D* **2**, 1 (1986).
- [43] H. Anderhub *et al.*, *Phys. Lett. B* **71**, 443 (1977).
- [44] P. O. Egan, S. Dhawan, V. W. Hughes, D. C. Lu, F. G. Mariam, P. A. Souder, J. Vetter, G. zu Putlitz, P. A. Thompson, and A. B. Denison, *Phys. Rev. A* **23**, 1152 (1981).
- [45] D. W. Norcross, *Comput. Phys. Commun.* **1**, 88 (1969).